Effect of strong magnetic fields on the nuclear "pasta" phase structure

R. C. R. de Lima,[1] S. S. Avancini,[2] and C. Providência[3]
[1]*Depto de Matemática, CCT, Universidade do Estado de Santa Catarina, Joinville, SC, 89219-710, Brazil*
[2]*Depto de Física, CFM, Universidade Federal de Santa Catarina, Florianópolis, SC, CP476, 88040-900, Brazil*
[3]*Centro de Física Computacional, Dep. de Física, Universidade de Coimbra, 3004-516, Coimbra, Portugal*
(Received 19 June 2013; published 13 September 2013)

The effect of strong magnetic fields on the properties of the pasta structure is calculated within a Thomas-Fermi approach using relativistic mean-field models to modulate stellar matter. It is shown how quantities such as the size of the clusters and Wigner-Seitz cells, the surface tension, and the transition between configurations are affected. It is expected that these effects may give rise to large stresses in the pasta phase if the local magnetic field suffers fluctuations.

DOI: 10.1103/PhysRevC.88.035804 PACS number(s): 21.65.Ef, 26.60.−c, 97.60.Jd

I. INTRODUCTION

In the bottom of the inner crust of proto-neutron and neutron stars, where the transition to the homogeneous core matter occurs, the existence of a special matter known as the *pasta* phase is expected. This phase is a frustrated system that arises from the competition between the strong and the electromagnetic interactions [1–6]. The basic shapes of these structures were named according to their geometry, i.e., droplets (bubbles), rods (tubes), and slabs for three, two, and one dimensions, respectively [1]; and the ground-state configuration is the one that minimizes the free energy. The pasta phase has been studied within the Thomas-Fermi approximation at zero and finite temperatures within different parametrizations of the relativistic nonlinear Walecka model [7] and of the density-dependent hadronic model [8–10].

It is known that magnetars, neutron stars with very strong magnetic fields of the order of 10^{14}–10^{15} G at the surface, are sources of very energetic electromagnetic radiation, mainly, γ and x rays [11–13]. Presently, more than 20 of these objects have been detected, most of them as soft γ repeaters (SGRs) and anomalous x-ray pulsars (AXPs) [14]. It is not clear how strong is the magnetic field in the interior, but several studies seem to indicate that fields stronger than 10^{18} G are not allowed. According to the scalar virial theorem [15] the interior magnetic field strength could be as large as $B \sim (1\text{–}3) \times 10^{18}$ G. Similar values were obtained in [16] from general relativistic magneto-hydrostatic calculations, and in [17] where the vanishing of the pressure parallel to the field restricted homogeneously distributed fields to intensities below 10^{19} G.

In the present study we investigate the effect of the magnetic field on the pasta structure. In [18] a simple expression, dependent on two parameters and the magnetic field intensity at the surface, was proposed to modulate the magnetic field with density. Taking this expression as reference and fields that are not stronger than $\sim(1\text{–}3) \times 10^{18}$ G in the interior we may expect that fields on the order of 10^{17} G could exist in the inner crust of the star. We consider fields in the range 10^{16}–10^{18} G.

The present study is organized in the following way: in Sec. II the formalism is presented, in Sec. III results are discussed, and the main conclusions are drawn in Sec. IV.

II. FORMALISM

We describe the nuclear matter at the inner crust within a relativistic mean-field (RMF) approach, in which the nucleons interact via the exchange of mesons. The exchanged mesons are the isoscalar-scalar and vector mesons (σ and ω, respectively) and the isovector meson (ρ). We consider a system of protons and neutrons with mass M interacting with and through an isoscalar-scalar field ϕ with mass m_s, an isoscalar-vector field V^μ with mass m_v, an isovector-vector field $\mathbf{b}^\mu$ with mass m_ρ. We also include a system of electrons with mass m_e to obtain a charge neutral system. Protons and electrons interact through the electromagnetic field A^μ. The Lagrangian density reads

$$\mathcal{L} = \sum_{i=p,n} \mathcal{L}_i + \mathcal{L}_e + \mathcal{L}_\sigma + \mathcal{L}_\omega + \mathcal{L}_\rho + \mathcal{L}_\gamma, \tag{1}$$

where the nucleon Lagrangian reads

$$\mathcal{L}_i = \bar{\psi}_i[\gamma_\mu i D^\mu - M^*]\psi_i, \tag{2}$$

with

$$i D^\mu = i\partial^\mu - g_v V^\mu - \frac{g_\rho}{2}\vec{\tau}\cdot\mathbf{b}^\mu - e\frac{1+\tau_3}{2}A^\mu, \tag{3}$$

$$M^* = M - g_s\phi, \tag{4}$$

and the electron Lagrangian is given by

$$\mathcal{L}_e = \bar{\psi}_e[\gamma_\mu(i\partial^\mu + eA^\mu) - m_e]\psi_e, \tag{5}$$

and the meson Lagrangian densities are

$$\mathcal{L}_\sigma = \tfrac{1}{2}\left(\partial_\mu\phi\partial^\mu\phi - m_s^2\phi^2 - \tfrac{1}{3}\kappa\phi^3 - \tfrac{1}{12}\lambda\phi^4\right), \tag{6}$$

$$\mathcal{L}_\omega = \tfrac{1}{2}\left(-\tfrac{1}{2}\Omega_{\mu\nu}\Omega^{\mu\nu} + m_v^2 V_\mu V^\mu + \tfrac{1}{12}\xi g_v^4 (V_\mu V^\mu)^2\right), \tag{7}$$

$$\mathcal{L}_\rho = \tfrac{1}{2}\left(-\tfrac{1}{2}\mathbf{B}_{\mu\nu}\cdot\mathbf{B}^{\mu\nu} + m_\rho^2\mathbf{b}_\mu\cdot\mathbf{b}^\mu\right), \tag{8}$$

$$\mathcal{L}_\gamma = -\tfrac{1}{4}F_{\mu\nu}F^{\mu\nu}, \tag{9}$$

where the tensors are given by

$$\Omega_{\mu\nu} = \partial_\mu V_\nu - \partial_\nu V_\mu, \tag{10}$$

$$\mathbf{B}_{\mu\nu} = \partial_\mu\mathbf{b}_\nu - \partial_\nu\mathbf{b}_\mu - g_\rho(\mathbf{b}_\mu\times\mathbf{b}_\nu), \tag{11}$$

$$F_{\mu\nu} = \partial_\mu A_\nu - \partial_\nu A_\mu. \tag{12}$$

The parameters of the model are the nucleon mass M, three coupling constants g_s, g_v, and g_ρ, of the mesons to the

TABLE I. Nuclear matter properties of NL3 and TM1.

	NL3 [19]	TM1 [21]
$\rho_0(\mathrm{fm}^{-3})$	0.148	0.145
M^*/M	0.60	0.634
$\sigma(Y_p = 0.3)$ (MeV/fm^2)	0.481	0.492
$\sigma(Y_p = 0.5)$ (MeV/fm^2)	1.123	1.077

nucleons, the electron mass m_e, the masses of the mesons m_s, m_v, m_ρ, the electromagnetic coupling constant $e = \sqrt{4\pi/137}$, and the self-interacting coupling constants κ, λ, and ξ.

We use the sets of constants proposed for parametrizations NL3 [19] and TM1 [20,21]. The nuclear matter properties provided by these sets of parameters are displayed in Table I. Both parametrizations have been fitted to the ground-state properties of stable and unstable nuclei. TM1 includes a quartic term involving the ω meson which allows for a softer equation of state at larger densities. Both models have a symmetry energy slope at saturation that is presently considered too high. Nevertheless we have considered these two models as reference since they have been widely used and we expect that the general features obtained with these models will be valid for other models.

We will not consider the effect of the anomalous magnetic moment because its effect is only important for magnetic fields stronger than the ones considered in the present study [22,23].

III. THE THOMAS-FERMI APPROXIMATION

From the Euler-Lagrange formalism, we obtain from Eq. (1) the coupled equations of motion for the scalar, isoscalar-vector, isovector-vector, electromagnetic, and nucleon fields. For a static system, only the zero components of the vector fields and currents will be present and due to charge conservation only the third component of the ρ-field remains. Therefore, the equations of motion in the RMF approximation become

$$\left(-\nabla^2 + m_s^2\right)\phi(\mathbf{r}) = g_s\rho_s(\mathbf{r}) - \frac{1}{2}\kappa\phi^2(\mathbf{r}) - \frac{1}{6}\lambda\phi^3(\mathbf{r}), \quad (13)$$

$$\left(-\nabla^2 + m_v^2\right)V_0(\mathbf{r}) = g_v\rho_B(\mathbf{r}) - \frac{1}{3!}\xi g_v^4 V_0^3(\mathbf{r}), \quad (14)$$

$$\left(-\nabla^2 + m_\rho^2\right)b_0(\mathbf{r}) = \frac{g_\rho}{2}\rho_3(\mathbf{r}), \quad (15)$$

$$-\nabla^2 A_0(\mathbf{r}) = e[\rho_p(\mathbf{r}) - \rho_e(\mathbf{r})], \quad (16)$$

where ρ_B is the baryonic density, ρ_3 is the isospin density, ρ_p, ρ_n, and ρ_e are the proton, neutron, and electron densities, and ρ_s is the scalar density. These quantities are given by

$$\begin{aligned}
\rho_B(\mathbf{r}) &= \rho_p(\mathbf{r}) + \rho_n(\mathbf{r}) = \langle\hat{\psi}^\dagger\hat{\psi}\rangle,\\
\rho_3(\mathbf{r}) &= \rho_p(\mathbf{r}) - \rho_n(\mathbf{r}) = \langle\hat{\psi}^\dagger\tau_3\hat{\psi}\rangle,\\
\rho_s(\mathbf{r}) &= \rho_{s_p}(\mathbf{r}) + \rho_{s_n}(\mathbf{r}) = \langle\hat{\bar{\psi}}\hat{\psi}\rangle,\\
\rho_e(\mathbf{r}) &= \langle\hat{\psi}_e^\dagger\hat{\psi}_e\rangle,
\end{aligned} \quad (17)$$

where $\langle\rangle$ stands for the expectation values of the field operators.

The nucleon field operators $\hat{\psi}^\dagger$ and $\hat{\psi}$ are expanded in a single-particle basis which for infinity nuclear matter in the mean-field approximation are plane wave states since the system is translationally invariant. In this work, as usual, the negative energy states will be neglected (no-sea approximation). We assume that matter consists of neutrons, protons, and electrons in a strong external homogeneous magnetic field $\mathbf{B}$ in the z direction. The gauge is fixed defining the 4-vector:

$$A^\mu = (0, 0, Bx, 0), \quad (18)$$

where we have $\mathbf{B} = B\,\hat{z}$ and $\nabla\cdot\mathbf{A} = 0$. At zero temperature all particle densities are calculated by occupying all single-particle levels in the positive energy Fermi sea until the Fermi level. These single-particle levels are solutions of a Dirac equation where the motion is free along the $\mathbf{B}$ field direction and quantized in the plane perpendicular to the field, yielding the Landau quantization [24]. The energy dispersion relations for charged particles are modified by the presence of the strong magnetic field [23] which breaks the rotational symmetry, and for the proton and electron they are given by

$$\epsilon^p = \sqrt{p_z^2 + \tilde{m}_p^2} + g_v V_0 + \tfrac{1}{2}g_\rho b_0 + eA_0, \quad (19)$$

$$\epsilon^e = \sqrt{p_z^2 + \tilde{m}_e^2} - eA_0, \quad (20)$$

where

$$\tilde{m}_p^2 = M^{\star 2} + 2\nu_p eB, \quad \tilde{m}_e^2 = {m_e}^2 + 2\nu_e eB, \quad (21)$$

$$\nu_i = \left(n + \frac{1}{2} - \frac{1}{2}\frac{q_i}{|q_i|}\sigma_z\right), \quad i = p, e, \quad \nu_i = 0, 1, 2, \ldots, \quad (22)$$

where $\sigma_z = \pm 1$ is the spin component along the magnetic field direction; $n = 0, 1, 2, \ldots$; q_i with $i = p, e$ stands for the electric charge of the proton and electron, respectively; and ν_i, $i = p, e$ is called the Landau level. Note that the spin degeneracy is 1 for the $\nu = 0$ Landau level and 2 for $\nu > 0$. Therefore, the modified density of states for a spin-1/2 charged particle becomes

$$2\int\frac{d^3p}{(2\pi)^3} \to \sum_{\sigma_z=\pm1}\sum_{n=0}^{\infty}\int\frac{eB}{(2\pi)^2}dp_z = \sum_{\nu=0}^{\infty} g_\nu\int\frac{eB}{(2\pi)^2}dp_z, \quad (23)$$

where $g_\nu = 1$ for $\nu = 0$ and 2 for $\nu > 0$. For zero temperature and charged particles, the number and energy densities read

$$\rho_i = \frac{eB}{2\pi^2}\sum_{\nu=0}^{\nu_{\max}} g_\nu p_{F,\nu}^i, \quad i = p, e, \quad (24)$$

$$\epsilon_i = \frac{eB}{(2\pi)^2}\sum_{\nu=0}^{\nu_{\max}} g_\nu\left[p_{F,\nu}^i\varepsilon_F^i + \tilde{m}_i^2\ln\left(\frac{p_{F,\nu}^i + \varepsilon_F^i}{p_{F,\nu}^i}\right)\right], \quad (25)$$

where $p_{F,\nu}^i$, $i = p, n$, is the Fermi momentum associated with the level with quantum number ν, and ε_F^i is the corresponding Fermi energy (or effective chemical potential). The Fermi momenta for the proton and electron are given by

$$p_{F,\nu}^p = \left[\left(\varepsilon_F^p\right)^2 - (M^\star)^2 - 2\nu_p eB\right]^{\frac{1}{2}}, \quad (26)$$

$$p_{F,\nu}^e = \left[\left(\varepsilon_F^e\right)^2 - m_e^2 - 2\nu_e eB\right]^{\frac{1}{2}}, \quad (27)$$

and the condition $p^i_{F,\nu} \geqslant 0$ sets an upper limit $\nu_{\max}$ in the summations:

$$\nu_{\max} = \left[\frac{\left(\varepsilon^p_F\right)^2 - (M^\star)^2}{2eB}\right], \quad \text{proton},$$
$$\nu_{\max} = \left[\frac{\left(\varepsilon^e_F\right)^2 - m_e^2}{2eB}\right], \quad \text{electron}, \tag{28}$$

where $[x]$ means the largest integer smaller or equal to x. For the neutron, one obtains the standard expressions [25]

$$\rho_n = \frac{\left(p^n_F\right)^3}{3\pi^2},$$
$$\epsilon_n = \frac{1}{8\pi^2}\left[2p^n_F\varepsilon^{n3}_F - M^{\star 2}p^n_F\varepsilon^n_F - M^{\star 4}\ln\left(\frac{p^n_F + \varepsilon^n_F}{M^\star}\right)\right]. \tag{29}$$

In the Thomas-Fermi approximation in close analogy to the density functional formalism, we assume that the meson fields vary sufficiently slowly so that the baryons are considered to be moving in locally constant fields. Therefore, locally the densities are calculated by plane waves instead of the true position-dependent single-particle states. Hence, we obtain the density of nucleons described by a Fermi gas with position-dependent Fermi momentum. Energy and particle densities become position dependent and the Thomas-Fermi equations at $T = 0$ are obtained from the extremization of the functional

$$\Omega = E_{\rm TF} - \sum_{i=p,n,e}\mu_i\int d^3r\rho_i(\vec{r}), \tag{30}$$

as a function of the Fermi momenta (or equivalently a function of the densities) in complete analogy with the density functional method. The Lagrange multipliers μ_i, $i = p, n, e$ are introduced in order to fix the number of particles due to species conservation. The Thomas-Fermi energy is given by

$$E_{\rm TF} = \int \epsilon(\vec{r})\, d^3r, \tag{31}$$

where

$$\epsilon(\vec{r}) = \sum_{i=p,n,e}\epsilon_i(\vec{r}) + \frac{1}{2}e(\rho_p - \rho_e)A_0(\vec{r}) + g_v(\rho_p + \rho_n)V_0(\vec{r}) + \frac{1}{2}g_\rho(\rho_p - \rho_n)b_0(\vec{r}) + \frac{1}{2}\left[(\vec{\nabla}\phi)^2 + m_s^2\phi^2\right] + \frac{\kappa}{3!}\phi^3 + \frac{\lambda}{4!}\phi^4 - \frac{1}{2}\left[(\vec{\nabla}V_0)^2 + m_v^2V_0^2\right] - \frac{1}{4!}\xi g_v^4V_0^4 - \frac{1}{2}\left[(\vec{\nabla}b_0)^2 + m_\rho^2b_0^2\right] - \frac{1}{2}[(\vec{\nabla}A_0)^2 - B^2]. \tag{32}$$

From the condition of extremum, one obtains the Thomas-Fermi equations

$$\mu_p = \sqrt{p^p_{F,\nu}(\vec{r})^2 + \tilde{m}_p(\vec{r})^2} + g_vV_0(\vec{r}) + \tfrac{1}{2}g_\rho b_0(\vec{r}) + eA_0(\vec{r}), \tag{33}$$

$$\mu_e = \sqrt{p^e_{F,\nu}(\vec{r})^2 + \tilde{m}_e^2} - eA_0(\vec{r}), \tag{34}$$

$$\mu_n = \sqrt{p^{n2}_F(\vec{r}) + M^\star(\vec{r})^2} + g_vV_0(\vec{r}) - \tfrac{1}{2}g_\rho b_0(\vec{r}). \tag{35}$$

To describe the properties of the inhomogeneous (pasta) phase we use the Wigner-Seitz approximation where the matter consisting of neutrons, protons, and electrons is considered to be inside of a neutral Wigner-Seitz cell and the interaction between cells is neglected.

Other important quantities in the study of the *npe* nonuniform matter are the rms radius $\langle r_i\rangle \equiv \sqrt{\bar{r_i^2}}$, where

$$\bar{r_i^2} = \int r^2\rho_i(r)\, r^d dr \Big/ \int \rho_i(r)\, r^d dr\ , \tag{36}$$

with $i = n, p, e$, and $d = 0, 1, 2$ for slabs, rods, or droplets, respectively; the neutron-skin thickness given by

$$\Theta = \langle r_n\rangle - \langle r_p\rangle; \tag{37}$$

and the surface energy defined as [10,26]

$$\sigma = \int_0^\infty dr\left[\left(\frac{d\phi_0}{dr}\right)^2 - \left(\frac{dV_0}{dr}\right)^2 - \left(\frac{db_0}{dr}\right)^2\right]. \tag{38}$$

IV. RESULTS AND DISCUSSIONS

In the following we discuss the effect of the magnetic field on several properties of the pasta clusters. We will consider electrically neutral matter with a fixed fraction of protons. For most of the examples we consider the fraction $Y_p = 0.3$ a reference value in supernova matter or proton-neutron matter, but we will also show results for $Y_p = 0.1$ a typical value of β-equilibrium neutron star matter. The magnetic field is along the rod axis in the rod geometry, and for the slab geometry in a direction perpendicular to the slab thickness.

It has been shown previously that Landau quantization softens the equation of state (EOS) due to the large degeneracy of the Landau levels [23,27]. Therefore, we expect that the free energy per particle will decrease in the presence of an external strong magnetic field. This is illustrated in Figs. 1 and 2, where the free energy per particle is given as a function of the density for different values of B. The homogeneous matter free energy per particle is plotted as function of the density for

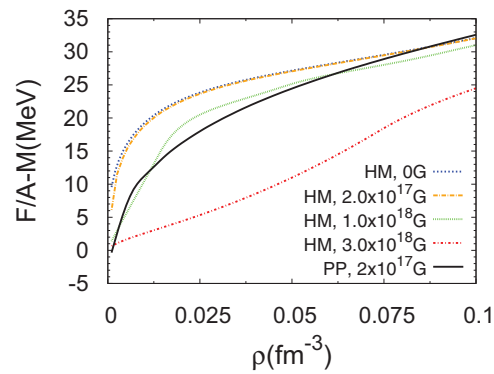

FIG. 1. (Color online) Energy per particle homogeneous *npe* neutral matter (HM) with $Y_p = 0.3$ vs density for different values of the magnetic field intensity. The calculation was performed with the NL3 parametrization. For comparison the energy per particle obtained for the pasta phase (PP) calculation with $B = 2 \times 10^{17}$ G is also included.

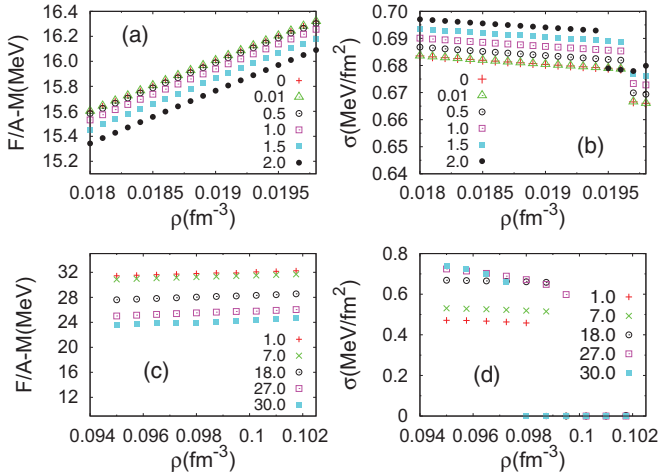

FIG. 2. (Color online) Free energy per particle (left) and surface energy (right) for the NL3 parametrization and $Y_p = 0.3$ at the droplet-rod transition (a,b) and the bubble-homogeneous transition (c,d). The calculations were performed for different values of the magnetic field intensity (B). The B units are 10^{17} G. Here the *free energy* is the energy itself as the system is assumed at temperature $T = 0$.

different values of the magnetic field (Fig. 1). For reference. we include in this same figure the results obtained within a pasta phase calculation for $B = 2 \times 10^{17}$ G, indicating that the free energy is lower and therefore that this configuration is favored. We conclude that the free energy per particle decreases when the magnetic field intensity increases and that in this range of densities nonhomogeneous matter is favored. For the pasta calculation (Fig. 2), two density ranges have been chosen: densities close to the drop-rod transition and the bubble-core transition. For $B = 5 \times 10^{16}$ G, the effect, on the order of 0.01%, is negligible. However, for $B = 2 \times 10^{17}$ G the free energy is 2% lower than for magnetic field free configurations. At the configuration transition the free energy is continuous; however, the surface energy defined by Eq. (38) suffers a jump. At the crust-core transition it goes to zero while at the drop-rod transition it suffers a small decrease. This discontinuity is possibly due not to the presence of a magnetic field but to the limitation of the calculation that only considers configurations with well-defined symmetries while intermediate geometries and shapes are expected to exist [28,29]. However, the magnetic field may change the transition density. This does not show a systematic trend, reflecting the filling of Landau levels and suffering a larger effect for larger magnetic fields.

In Fig. 3 the transition densities between the geometries droplet-rod (left) and tube-bubble (right) are plotted as a function of the field intensity. The transition density between different geometries suffers fluctuations that can be as high as 5% when the field changes between 10^{17} and 10^{18} G. However, taking fields not larger than 2×10^{17} the effect on the transition between geometries is a reduction of the transition density not larger than 1.5%.

An increase of the binding energy between the nucleons gives rise to a larger surface energy, which may affect the

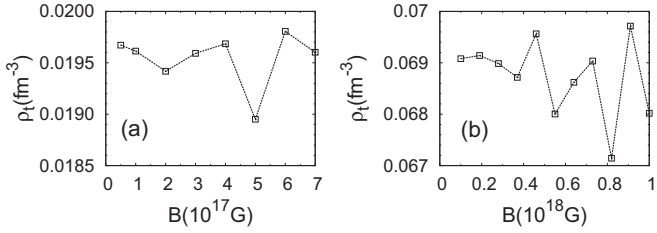

FIG. 3. Transition density for NL3 and $Y_p = 0.3$: (a) droplet-rod; (b) tube-bubble.

pasta structure, namely, the radius of the clusters, the crust-core transition, and the transition between different configurations. Moreover, Landau quantization may also give origin to large fluctuations. In Fig. 4 the surface energy is plotted for parametrizations NL3 and TM1 and a proton fraction $Y_p = 0.3$ for a slab configuration at $\rho = 0.06$ fm^{-3} as a function of the magnetic field intensity. The main trend is an increase of the surface energy with the magnetic field. For a field on the order of 10^{18} G, which probably is already too strong in the inner crust, the surface energy is 20% larger when compared with the no field case. A 2×10^{17} G field gives rise to an effect 10 times smaller, on the order of $\sim 2\%$. These conclusions are confirmed by the top right panel of Fig. 2 where the surface energy is plotted as a function of the density at the drop-rod transition.

In Fig. 5 results for the bubble configuration, including the Coulomb interaction self-consistently, are plotted including the surface energy, and the radius of the Wigner-Seitz cell. These results were obtained for NL3 with the proton fraction $Y_p = 0.3$ at $\rho = 0.095$ fm^{-3}. As already discussed, there is a clear increase of the surface energy with the magnetic field intensity which can be as large as 50% for $B = 3 \times 10^{18}$ G. Small fluctuations of the surface energy reflect themselves on the Wigner-Seitz cell radius and total nucleon number inside the cluster. These effects are more dramatic above $B = 10^{18}$ G, but at $B \sim 2 \times 10^{17}$G effects of 5–10% are already expected.

In Fig. 6 the surface energy is plotted for densities below the the drop-rod transition, and two proton fractions $Y_p = 0.3$ and

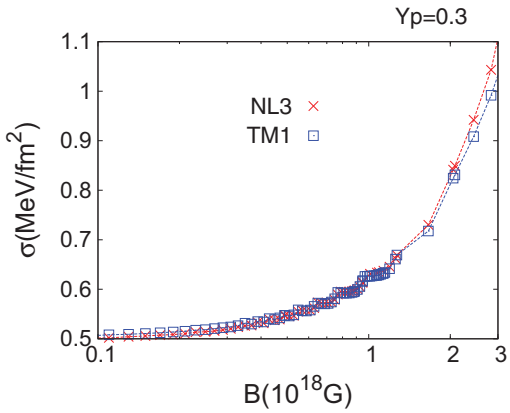

FIG. 4. (Color online) Surface energy defined by the Eq. (38) as a function of the magnetic field for $Y_p = 0.3$, obtained with NL3 and TM1 parametrizations and the slab configuration with the Coulomb interaction switched off for $\rho = 0.06$ fm^{-3}.

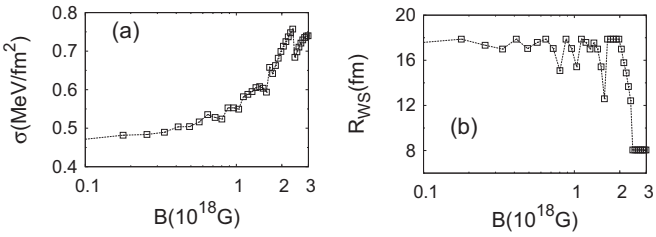

FIG. 5. Calculations for the bubble geometry, NL3 parametrization, $Y_p = 0.3$, and $\rho_B = 0.095$ fm^{-3}: (a) surface energy; (b) Wigner-Seitz radius.

0.1. For the larger proton fraction we get a behavior similar to the one previously discussed, namely, an increase of the surface energy with the increase of the field strength. The surface energy is larger for the smaller densities because clusters are smaller and the neutron dripped gas is smaller. Decreasing the proton fraction to $Y_p = 0.1$ this last feature is still present (see Fig. 7); however, the surface energy suffers a small decrease for fields below 10^{18}G and only increases for stronger fields.

In Fig. 8 are shown the density profiles of the configurations used to calculate the surface energy for both proton fractions: for $Y_p = 0.3$ the thickness of the droplet surface decreases with B, while for $Y_p = 0.1$ there is an increase of the surface thickness from 10^{17} to 5×10^{17}G followed by a decrease for still larger fields. The number of Landau levels filled with the proton and electron distributions for each field are given in Fig. 9. A smaller number of levels is involved for the smaller proton fraction, and, therefore, $Y_p = 0.1$ is more sensitive to strong magnetic fields. The calculation of the surface energy reflects the size of the cluster, its proton fraction, and the interaction between particles. For $Y_p = 0.3$ the size of the cluster is practically not affected as seen in Fig. 8, and therefore σ will essentially give information about the binding between particles. On the other hand, Fig. 8 shows that if $Y_p = 0.1$ the neutron distribution is quite affected by the interaction change the protons feel in the presence of the magnetic field. On the

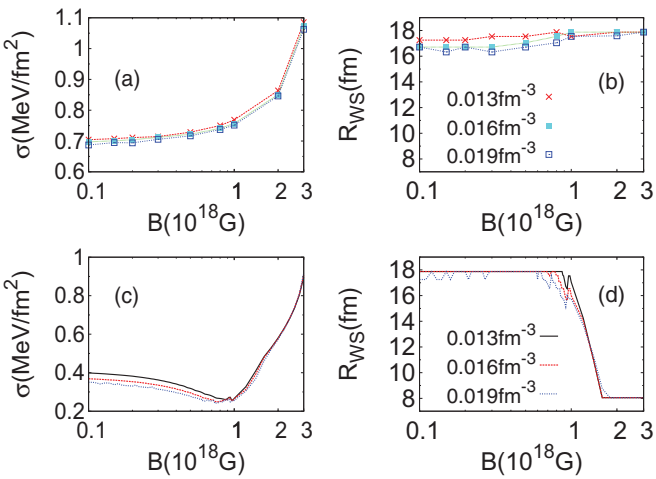

FIG. 6. (Color online) Surface energy (left) and Wigner-Seitz radius (right), for the droplet geometry, NL3 parametrization, baryonic density $\rho = 0.019$ fm^{-3}, and proton fraction: (a,b) $Y_p = 0.3$; (c,d) $Y_p = 0.1$.

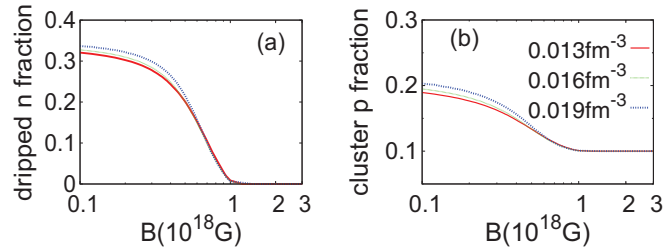

FIG. 7. (Color online) Results in the pasta cluster for $Y_p = 0.1$: (a) dripped neutron fraction; (b) proton fraction.

whole for weaker fields the surface energy decreases with B. For the larger magnetic fields no neutrons drip out and the proton fraction of the droplet becomes 0.1. This very small fraction of protons favors smaller droplets, because a large asymmetry term reduces the stability of the clusters.

In fact, increasing the magnetic field intensity changes the structure of the droplet pasta phase for a proton fraction $Y_p = 0.1$, eliminating completely the neutron dripped gas (see Fig. 7) and making the clusters less proton rich. A direct consequence is the transition to the rod geometry driven by magnetic field.

In Fig. 10 the average radius of the distribution of neutrons and electrons inside a spherical cluster is plotted for a set of densities close to the droplet-rod transition calculated according to Eq. (36). The main effect of the magnetic field shows itself on the neutron distribution with an average radius that decreases with B. Due to an increase of the surface energy, neutrons do not drip so easily and therefore the number of neutrons outside the cluster is smaller. Electrons

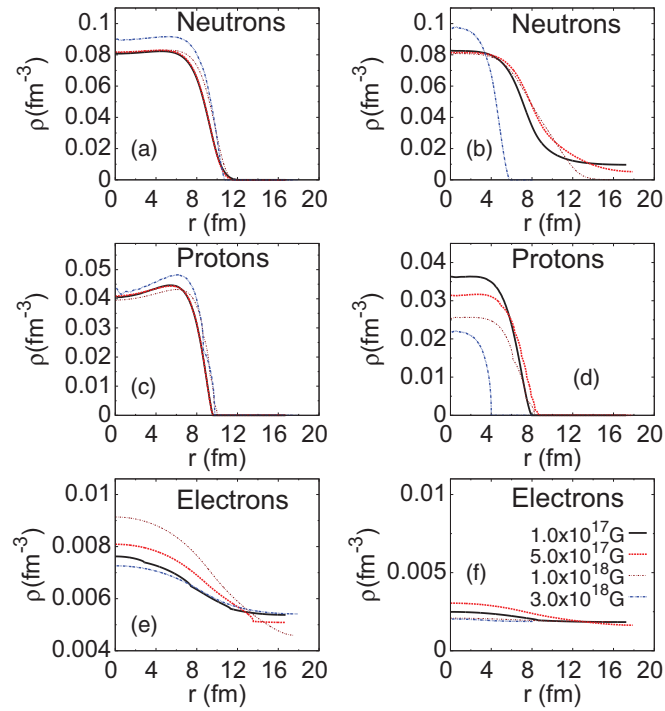

FIG. 8. (Color online) Density profile in the Wigner-Seitz cell for the droplet geometry, NL3 parametrization, proton fraction $Y_p = 0.3$ (left) and $Y_p = 0.1$ (right) for baryonic density $\rho = 0.019$ fm^{-3} for neutrons, protons, and electrons.

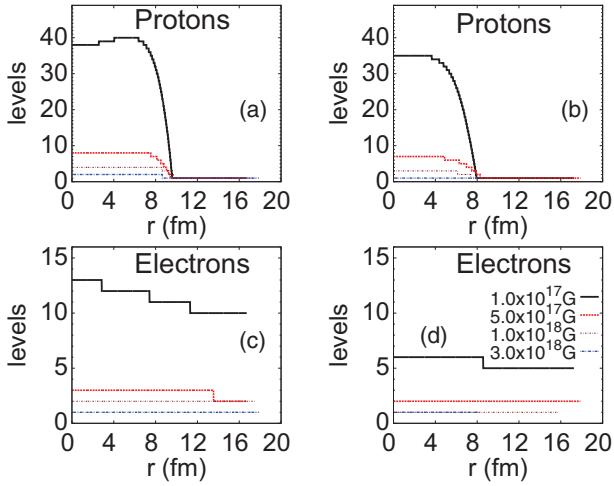

FIG. 9. (Color online) Landau levels in the Wigner-Seitz cell for the droplet geometry, NL3 parametrization, proton fraction $Y_p = 0.3$ (left) and $Y_p = 0.1$ (right) for the baryonic density $\rho = 0.019$ fm^{-3} for protons and electrons.

are particularly sensitive to magnetic fields as strong as 10^{17}–10^{18} G due to their small mass. The filling of Landau levels gives rise to the fluctuations shown on the right panel of Fig. 10. This is a manifestation of the De Haas–van Alphen effect.

It is seen that the distribution of electrons is not flat and a self-consistent calculation that takes into account correctly charge distribution will be affected by the magnetic field. In particular, the rearrangement of the proton distributions will give rise to smaller proton fractions at the cluster center and smaller neutron skins. The effect on the neutron skins is seen in Fig. 11 where the neutron-skin thickness calculated with NL3 for $Y_p = 0.3$ and densities close to the drop-rod transition, according to Eq. (37), is plotted. There is a decrease of about 3–4% when the field increases from 5×10^{16} to 2×10^{17} G. Above $B = 10^{17}$ G the oscillations present are a consequence of the Landau quantization of the proton energy levels.

We next analyze the effect of the magnetic field on the crust-core transition. The evolution of the Wigner-Seitz radius and particle distributions inside the cell with the magnetic field is plotted in Fig. 12 for two bubble configurations, at $\rho = 0.095$ and 0.0995 fm^{-3}, the second one close to the crust-core transition. For $10^{17} < B < 10^{18}$ G and $\rho = 0.095$ fm^{-3}, the variation of $R_{\rm WS}$ is small and becomes more pronounced for

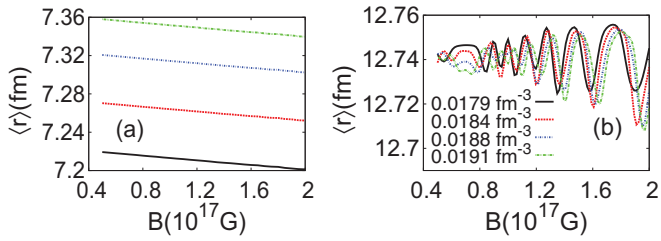

FIG. 10. (Color online) Average radius for the droplet geometry, NL3 parametrization, and proton fraction $Y_p = 0.3$: (a) neutrons; (b) electrons.

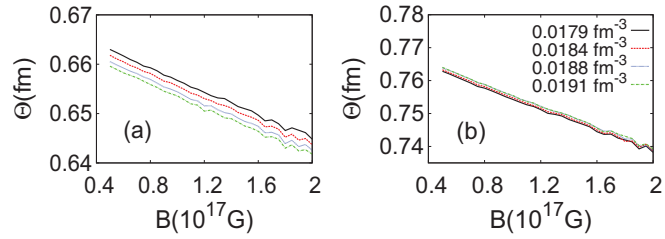

FIG. 11. (Color online) Neutron-skin thickness for NL3 and $Y_p = 0.3$ for densities close to the drop-rod transition: (a) droplet geometry; (b) rod geometry.

stronger fields. However, the effect of B on the surface energy is clearly seen, which gives rise to a narrower surface thickness, larger central densities, and smaller tails at the bubble center. This is true for both neutrons and protons. As expected due to their much smaller mass, the electron distributions are more sensitive to the field intensity.

The density $\rho = 0.0995$ fm^{-3} is very close to the crust-core transition, and the filling of the Landau levels may dictate that for a given B the transition to the core has already occurred ($B = 6.8 \times 10^{17}$ G) while for other intensities a more pronounced bubble occurs with smaller electron densities in the center of the bubble ($B \sim 10^{18}$ G). For $B = 3 \times 10^{18}$ G a configuration very close to the crust-core transition occurs. The transition density to the homogeneous phase suffers essentially an increase that will be about 1% for 2×10^{17} G and can go up to 5% for $B = 10^{18}$ G, see Fig. 13.

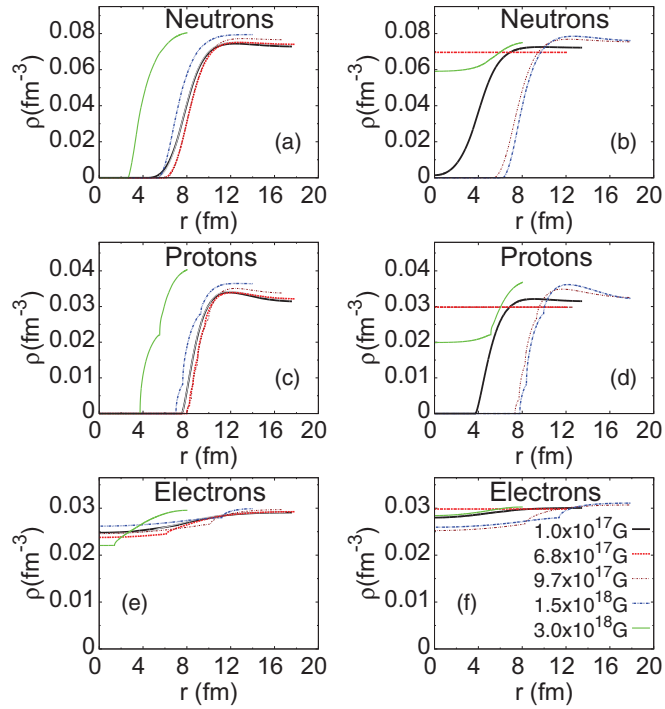

FIG. 12. (Color online) Density profile in the Wigner-Seitz cell for the bubble geometry, NL3 parametrization, proton fraction $Y_p = 0.3$, and baryonic density $\rho = 0.095$ fm^{-3} (left) and $\rho = 0.0995$ fm^{-3} (right) for neutrons, protons, and electrons.

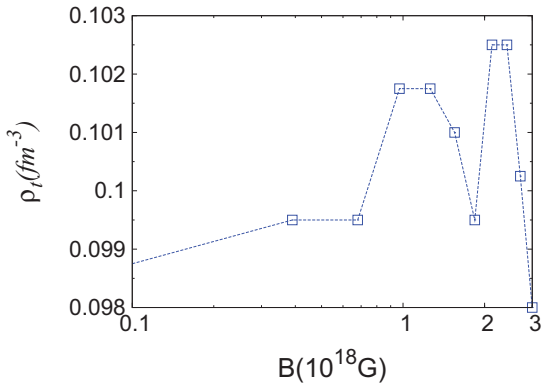

FIG. 13. (Color online) Transition density at the bubble-homogeneous matter, for NL3 $Y_p = 0.3$.

Magnetic field fluctuations may give rise to nonequilibrium configurations that will tend to evolve in time to equilibrium configurations originating inner tensions that could give rise to star quakes and bursting activity of magnetars.

V. CONCLUSION

In the present study the effect of the magnetic field on the pasta phase calculated within a Thomas-Fermi formalism has been discussed. Nuclear matter was described mostly by the RMF parametrization NL3 and proton fractions of 0.3 and 0.1 were considered.

Our main aim was to determine how the magnetic field could affect the free energy per particle, the radius of the Wigner-Seitz cells, the cluster properties, and the transitions between different configurations, or the crust-core transition. Most of the calculations were done for fields below 10^{18} G, although, in order to estimate upper limits, some of the calculations were pushed to 3×10^{18} G.

It is known that the pasta phase is a frustrated system that results from the competition between the Coulomb and the surface energy. It is, therefore, expected that this phase will be affected by a strong magnetic field. Charged particles in a magnetic field suffer the Landau quantization, which gives rise to a decrease of the free energy per particle due to the large degeneracy levels in the direction perpendicular to the field and, therefore, to an increase of the surface energy. The surface thickness of clusters will be thinner, the inner densities larger, and, since neutrons will not drip off so easily, a smaller number of particles will occur in the background gas. We have also shown that the transition between different configurations or crust-core will be affected although in an irregular way. Fluctuations of the magnetic field may give rise to inner stresses that oblige the system to evolve to an equilibrium configuration and originate bursting activity of magnetars.

The present work was just exploratory and a more careful study should be done that uses models with a symmetry energy that satisfies experimental constraints and considers smaller proton fractions, namely, β-equilibrium stellar matter. A study of the stress developed on these structures should also be performed.

ACKNOWLEDGMENTS

This work was partially supported by COMPETE/FEDER and FCT (Portugal) under Grant No. PTDC/FIS/113292/2009, CNPQ (Brazil) and Capes/FCT (Brazil) under Project No. 232/09, and FAPESC (Brazil) under Grant No. 6316/2011-9.

[1] D. G. Ravenhall, C. J. Pethick, and J. R. Wilson, Phys. Rev. Lett. **50**, 2066 (1983).
[2] M. Hashimoto, H. Seki, and M. Yamada, Prog. Theor. Phys. **71**, 320 (1984).
[3] C. J. Horowitz, M. A. Pérez-Garcia, and J. Piekarewicz, Phys. Rev. C **69**, 045804 (2004); **72**, 035801 (2005).
[4] T. Maruyama, T. Tatsumi, D. N. Voskresensky, T. Tanigawa, and S. Chiba, Phys. Rev. C **72**, 015802 (2005).
[5] G. Watanabe, K. Sato, K. Yasuoka, and T. Ebisuzaki, Phys. Rev. C **66**, 012801 (2002); **68**, 035806 (2003); **69**, 055805 (2004); H. Sonoda, G. Watanabe, K. Sato, K. Yasuoka, and T. Ebisuzaki, *ibid*. **77**, 035806 (2008).
[6] F. Grill, C. Providência, and S. S. Avancini, Phys. Rev. C **85**, 055808 (2012).
[7] J. Boguta and A. R. Bodmer, Nucl. Phys. A **292**, 413 (1977).
[8] S. S. Avancini, D. P. Menezes, M. D. Alloy, J. R. Marinelli, M. M. W. Moraes, and C. Providência, Phys. Rev. C **78**, 015802 (2008).
[9] S. S. Avancini, L. Brito, J. R. Marinelli, D. P. Menezes, M. M. W. de Moraes, C. Providência, and A. M. Santos, Phys. Rev. C **79**, 035804 (2009).
[10] S. S. Avancini, S. Chiacchiera, D. P. Menezes, and C. Providência, Phys. Rev. C **82**, 055807 (2010); **85**, 059904(E) (2012).
[11] R. C. Duncan and C. Thompson, Astrophys. J. **392**, L9 (1992); C. Thompson and R. C. Duncan, Mon. Not. R. Astro. Soc. **275**, 255 (1995).
[12] V. V. Usov, Nature (London) **357**, 472 (1992).
[13] B. Paczyński, Acta Astron. **42**, 145 (1992).
[14] McGill SGR/AXP Online Catalog, http://www.physics.mcgill.ca/~pulsar/magnetar/main.html.
[15] D. Lai and S. Shapiro, Astrophys. J. **383**, 745 (1991).
[16] A. E. Broderick, M. Prakash, and J. M. Lattimer, Phys. Lett. B **531**, 167 (2002).
[17] M. Sinha, B. Mukhopadhyay, and A. Sedrakian, Nucl. Phys. A **898**, 43 (2013).
[18] D. Bandyopadhyay, S. Chakrabarty, and S. Pal, Phys. Rev. Lett. **79**, 2176 (1997).
[19] G. A. Lalazissis, J. König, and P. Ring, Phys. Rev. C **55**, 540 (1997).
[20] K. Sumiyoshi, H. Kuwabara, and H. Toki, Nucl. Phys. A **581**, 725 (1995).
[21] Y. Sugahara and H. Toki, Nucl. Phys. A **579**, 557 (1994).

[22] A. Rabhi, C. Providência and J. da Providência, J. Phys. G **35**, 125201 (2008).
[23] A. Broderick, M. Prakash, and J. M. Lattimer, Astrophys. J. **537**, 351 (2000).
[24] L. D. Landau and E. M. Lifshitz, *Quantum Mechanics*, A Course of Theoretical Physics Vol. 3 (Pergamon, New York, 1965).
[25] H. Müller and B. D. Serot, Phys. Rev. C **52**, 2072 (1995).
[26] D. P. Menezes and C. Providência, Phys. Rev. C **60**, 024313 (1999)
[27] A. Rabhi, C. Providência, and J. Da Providência, Phys. Rev. C **79**, 015804 (2009); Aziz Rabhi and C. Providência, J. Phys. G: Nucl. Part. Phys. **37**, 075102 (2010).
[28] H. Pais and J. R. Stone, Phys. Rev. Lett. **109**, 151101 (2012).
[29] C. O. Dorso, P. A. Giménez Molinelli, and J. A. López, Phys. Rev. C **86**, 055805 (2012).